Delft University of Technology

Coupling Mesoscale Budget Components to Large-Eddy Simulations for Wind-Energy Applications

Draxl, Caroline; Allaerts, Dries; Quon, Eliot; Churchfield, Matt

DOI
[10.1007/s10546-020-00584-z](10.1007/s10546-020-00584-z)

Publication date
2021

Document Version
Final published version

Published in
Boundary-Layer Meteorology

Important note
To cite this publication, please use the final published version (if applicable).
Please check the document version above.

RESEARCH ARTICLE

Coupling Mesoscale Budget Components to Large-Eddy Simulations for Wind-Energy Applications

Caroline Draxl[1,2] · **Dries Allaerts[1,3]** · **Eliot Quon[1]** · **Matt Churchfield[1]**

Abstract

To simulate the airflow through a wind farm across a wide range of atmospheric conditions, microscale models (e.g., large-eddy simulation, LES, models) have to be coupled with mesoscale models, because microscale models lack the atmospheric physical processes to represent time-varying local forcing. Here we couple mesoscale model outputs to a LES solver by applying mesoscale momentum- and temperature-budget components from the Weather Research and Forecasting model to the governing equations of the Simulator fOr Wind Farm Applications model. We test whether averaging the budget components affects the LES results with regard to quantities of interest to wind energy. Our study focuses on flat terrain during a quiescent diurnal cycle. The simulation results are compared with observations from a 200-m tall meteorological tower and a wind-profiling radar, by analyzing time series, profiles, rotor-averaged quantities, and spectra. While results show that averaging reduces the spatio-temporal variability of the mesoscale momentum-budget components, when coupled with the LES model, the mesoscale bias (in comparison with observations of wind speed and direction, and potential temperature) is not reduced. In contrast, the LES technique can correct for shear and veer. In both cases, however, averaging the budget components shows no significant impact on the mean flow quantities in the microscale and is not necessary when coupling mesocale budget components to the LES model.

✉ Caroline Draxl
  caroline.draxl@nrel.gov

1 National Renewable Energy Laboratory (NREL), 15013 Denver West Parkway, Golden, CO 80401, USA

2 Renewable and Sustainable Energy Institute (RASEI), Boulder, CO 80309, USA

3 Faculty of Aerospace Engineering, Delft University of Technology, Kluyverweg 1, 2629 HS Delft, The Netherlands

1 Introduction

Targeting reductions in the cost of wind energy through an improved understanding of the physics that govern electricity generation by wind farms is the overarching motivation of this research. One of the steps towards gaining this understanding is to use high-performance computing to perform high-fidelity large-eddy simulations (LES) of the flow through wind farms as accurately as possible across a wide range of atmospheric conditions. Through such simulations, an improved understanding of wind-farm performance can lead to new turbine designs and operation strategies that reduce the cost of wind energy. For example, researchers can use such simulations to study how new wind-farm control systems respond to frontal passages, or how next-generation, very large, and flexible offshore turbines handle hurricane wind speeds.

Wind farms are exposed to a wide range of weather phenomena and variabilities on many scales. Meteorological variability spans scales such as synoptic conditions, weather events, and terrain-driven diurnal variability. These variabilities can be captured using mesoscale numerical weather prediction models, which compute meteorological and topographical features at the mesoscale—a scale between O(10) and O(100) km and, hours to days. These features include fronts, low-level jets (LLJ), sea breezes, and thunderstorms. Mesoscale features drive large horizontal microscale variations, including the vertical structure of the atmospheric boundary layer (ABL), and hence the development of turbulence. The microscale, which denotes space and time scales smaller than 2 km and ranging from minutes to hours, respectively, modulates the operating environment of wind farms, leading to flow characteristics that can influence both power capture and fatigue loading (Haupt et al. 2015). As microscale models are able to simulate and resolve turbulence and microscale flow structures, they are able to describe the flow through wind farms in much more detail than the coarser mesoscale models. However, microscale models lack the atmospheric physical processes to represent local forcings such as radiation, clouds, precipitation, and surface fluxes. In order to represent a wide range of important meteorological phenomena, this mesoscale information needs to be available in microscale models to simulate the flow on all the atmospheric scales that affect wind-farm performance.

Mesoscale-to-microscale coupling (MMC) can be approached by using either a unified solver that supports mesh refinement and scale-appropriate physics modules (e.g., the Weather Research and Forecasting (WRF) model together with a LES solver; Mirocha et al. 2014, 2010; Muñoz-Esparza et al. 2014, 2017; Rai et al. 2019), or using a stand-alone microscale solver driven by forcing parameters from a mesoscale simulation (e.g., Gopalan et al. 2014; Castro et al. 2015; Heinze et al. 2017; Arroyo et al. 2018; Haupt et al. 2017). Furthermore, the coupling can be performed one-way (i.e., the mesoscale simulations provide input to the microscale but not vice versa) or two-way (in which the microscale solver provides feedback to the mesoscale simulation). The latter approach is difficult to achieve using a mesoscale model coupled to a stand-alone microscale code because mesoscale codes often solve the compressible Euler equations, whereas microscale codes typically solve the incompressible Navier–Stokes equations (Sprague and Satkauskas 2015), and the practical implementation for realistic cases cannot be found in the literature.

Mesoscale-to-microscale with a standalone microscale LES code can be further divided into two approaches. The first approach simulates a finite domain with Dirichlet inflow boundary conditions consisting of planes of spatio-temporally varying velocity and temperature sampled from planes within the mesoscale domain. Perturbations must be applied to this inflow data to initiate the resolved turbulence. The challenge is that, once the perturbations initiate resolved turbulence, the turbulence requires a few kilometres of fetch (Muñoz-Esparza

and Kosović 2018) and, thus, considerable extra computational cost to reach equilibrium. The second approach to coupling (which is the approach used here) is to use height–time varying mesoscale forcings on a laterally periodic domain. In this case, the situation is much more like a typical atmospheric LES, but with more sophisticated forcings. Here, perturbations are only needed at the start of a simulation to initiate turbulence (e.g., Muñoz-Esparza et al. 2014, 2015; Wu 2017; Quon et al. 2018; Muñoz-Esparza and Kosović 2018). Although there is an initial transient time over which realistic turbulence must develop, there is no persistent fetch over which turbulence develops. Mesoscale forcing is applied to the microscale LES in the entire horizontal extent of the microscale domain, as opposed to only the inflow boundaries. If, for example, a warm front were communicated from the mesoscale to the microscale, no temperature gradient would exist across the domain, but the whole microscale domain would heat up gradually. This approach is horizontally homogeneous and an appropriate approximation of fronts with weak horizontal gradients; however, its applicability to complex terrain requires further research. Both methods, using inflow planes and height–time varying forcing, further require mesoscale forcing of the geostrophic wind speeds, the aerodynamic roughness length z_0, and surface sensible heat flux or skin temperature. We refer to this technique as the budget-component coupling technique.

Another topic to consider regarding the MMC approach is at which horizontal resolution to communicate the mesoscale output to the microscale. This is especially important when mesoscale simulations fall into the so-called terra incognita (Wyngaard 2004), since ABL parametrizations assume that turbulent eddies are not explicitly resolved. At a grid resolution between about 100 m and the boundary-layer depth, this assumption fails, as some eddies may be resolved, and simulations can exhibit numerical artifacts. Wyngaard (2004) called this numerical region the terra incognita, which he estimated to be within the range 100–1000 m. Rai et al. (2019) found that mesoscale domains with grid spacing in the terra incognita do not have a large impact on the LES results, and that artifacts occur at grid spacing less than the boundary-layer depth. They conclude that the results in the microscale LES domain depend on the type of turbulence model used in the microscale domain itself rather than the grid spacing of the mesoscale domain. Their area of study was the same as ours, a flat terrain in Texas (Sect. 2.1), and their boundary-layer depth (and therefore analyzed grid spacing) was 1.6, 2.3, and 3.2 km. Since the grid spacing in our simulations is 3 km (at the upper end of the boundary-layer depths of Rai et al. 2019 and above Wyngaard's definition), we do not anticipate the terra incognita to influence our microscale results. However, Rai et al. (2019) used a unified solver that supports mesh refinement and scale-appropriate physics modules within one code base (i.e., the WRF model). In the future, we suggest considering the effects of mesoscale simulations in the terra incognita using the budget-component coupling technique.

Here, we use mesoscale momentum and temperature budget components as height–time varying forcing for mesocale effects for wind-energy applications over a diurnal cycle. Because microscale models usually do not account for physical processes affecting mesoscale weather (Allaerts et al. 2020), most LES studies of the ABL focused on idealized flows. Few have performed LES investigations over a full diurnal cycle (Duynkerke et al. 2004; Kumar et al. 2006, 2010; Kleissl et al. 2006; Basu et al. 2008a, b; Englberger and Dörnbrack 2018; Tian et al. 2020, with all, except Kumar et al. (2010), relying upon idealized forcing conditions, and none accounting for large-scale advection of momentum or temperature. For example, Muñoz-Esparza et al. (2017) simulated a diurnal cycle using a unified solver (the WRF model). The approach of using mesoscale budget components has been evaluated (Schalkwijk et al. 2015; Heinze et al. 2017; Sanz Rodrigo et al. 2017a, b; Olsen 2018), with both Heinze et al. (2017) and Sanz Rodrigo et al. (2017b) finding that larger-scale budget components should not contain small-scale information resolved by the LES model, but their

approach to exclude this information differs from ours. Heinze et al. (2017) coupled momentum budget components from the operational Consortium for Small Scale Modeling model at 2.8-km and 3-h resolution to two LES solvers and averaged the large-scale budget components horizontally and vertically (i.e., spatially). They analyzed LES results with respect to mean boundary-layer quantities without focusing on wind energy. Sanz Rodrigo et al. (2017b) averaged mesocale budget components temporally to 1-h values and used mesoscale output at 9-km resolution in a Reynolds-averaged Navier–Stokes single-column microscale model. Heinze et al. (2017) and Sanz Rodrigo et al. (2017b) analyzed the averaging techniques by analyzing budget components before they were coupled with the microscale solver. We apply the budget-component coupling technique to a standalone microscale LES solver and analyze the impact of non-averaged, spatially-averaged, and temporally-averaged momentum-budget components on the microscale solution. We couple the differently averaged budget components to an open-source LES solver and analyze the microscale model output for each case. Our aim is to demonstrate the utility of the budget-component MMC approach with the LES technique and to determine the best averaging technique for wind-energy applications.

We address the following hypotheses:

(i) Mesoscale models have difficulties predicting profiles of shear and veer. We anticipate, due to the general nature of the LES approach, that it can correct the mesoscale predictions for shear and veer but cannot adjust the wind speed and direction, as it is driven by the mesoscale trends.

Because there appears to be no consensus as to whether horizontal or temporal averaging yields the best results in the microscale, we also address the following hypotheses:

(ii) Sanz Rodrigo et al. (2017b) state that temporal and spatial averaging are required to remove unphysical noise from the budget-component time history and spatial field. We hypothesize that noise in the budget components is undesirable and that averaging provides more accurate flow fields.

(iii) If averaging of the budget components is performed, we hypothesize that spatial averaging is advantageous. By temporally averaging the forcing terms, flow features may be smoothed in certain weather situations (e.g., the exact timing of a cold front passage). This violates the sense of the MMC strategy, which is to integrate specific weather situations into the microscale model.

Below, we describe the models used to accomplish the MMC strategy, as well as the observations used to validate the microscale simulations, case selection, and the coupling methodology in Sect. 2. Section 3 describes mesoscale budget components and the microscale solution, using these as input over a diurnal cycle. Section 4 describes the impact of spatially- and temporally-averaged budget components on the microscale simulations, and we conclude our research in Sect. 5.

2 Case Selection, Model Set-up, and Methodology

Our study focuses on flat terrain conditions, in which the evolution of the ABL is mostly governed by mesoscale diurnal forcing. In the morning, as surface heating increases, the atmosphere becomes more convective, leading first to convective rolls which later can become convective cells, depending on the relative magnitudes of the mean wind speed and surface buoyant forcing. The daytime convection collapses with the setting of the sun when the surface heat flux diminishes and becomes negative. Before becoming stable, the boundary layer becomes neutral for a very brief period. At night, the stable boundary layer is characterized
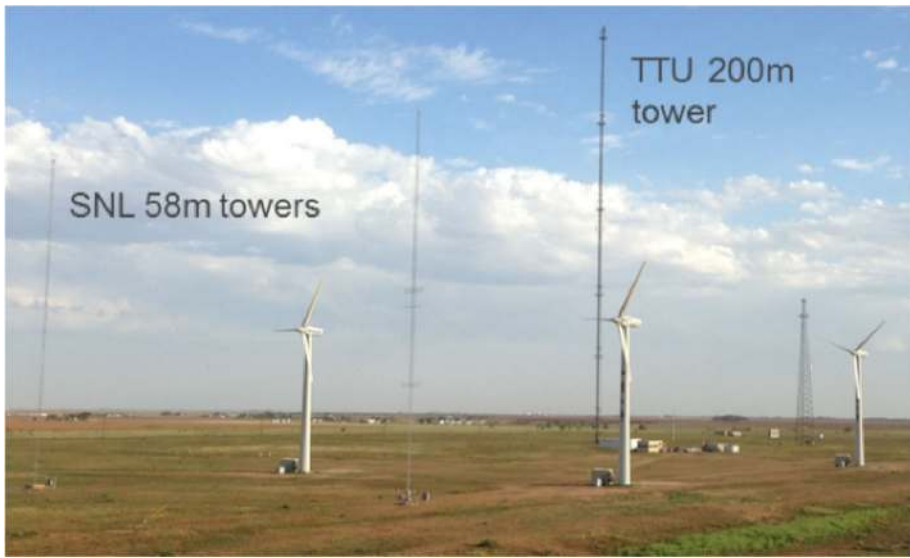
Fig. 1 Photograph of Department of Energy/Sandia National Laboratories (SNL) SWiFT Experimental Wind Farm Facility, which includes three turbines and adjacent TTU atmospheric facilities

by relatively low boundary-layer heights, smaller-scale turbulence, and the potential for LLJ formation. At sunrise, the boundary layer once again transitions through the neutral state before becoming unstable and convective.

When coupling microscale turbulence-resolving simulations with mesoscale simulations containing no resolved turbulence (mesoscale solvers completely parametrize the turbulence within the ABL), the initiation of turbulence is one of the biggest challenges to overcome. The success of developing realistic turbulent structures in the microscale varies with different atmospheric stability conditions occurring during a diurnal cycle. Moreover, simulating the transition between these stability conditions may pose additional challenges. For these reasons, we investigate a diurnal cycle which captures the development and transitions of the convective and stable ABL over flat terrain. The particular location and date considered here are discussed in Sect. 2.1, after which the mesoscale and microscale solvers are described in Sects. 2.2 and 2.3, respectively. Details of the coupling methodology are provided in Sect. 2.4.

2.1 Case Selection

The U.S. Department of Energy and Sandia National Laboratories Scaled Wind Farm Technology (SWiFT) facility was selected as a test site for MMC simulations. The SWiFT site is located in the southern Great Plains in west Texas with surrounding grassland and small bushes; the location has very minor terrain changes and no significant geographic features for hundreds of miles (Fig. 1). In addition to its ideal terrain, the SWiFT site was also chosen for its relevance to wind-energy installations in the U.S.A. and for the adjacent meteorological measurement facilities hosted by Texas Tech University's (TTU) National Wind Institute. Detailed information on the SWiFT site and National Wind Institute measurement facilities can be found in Hirth and Schroeder (2014), and Kelley and Ennis (2016).
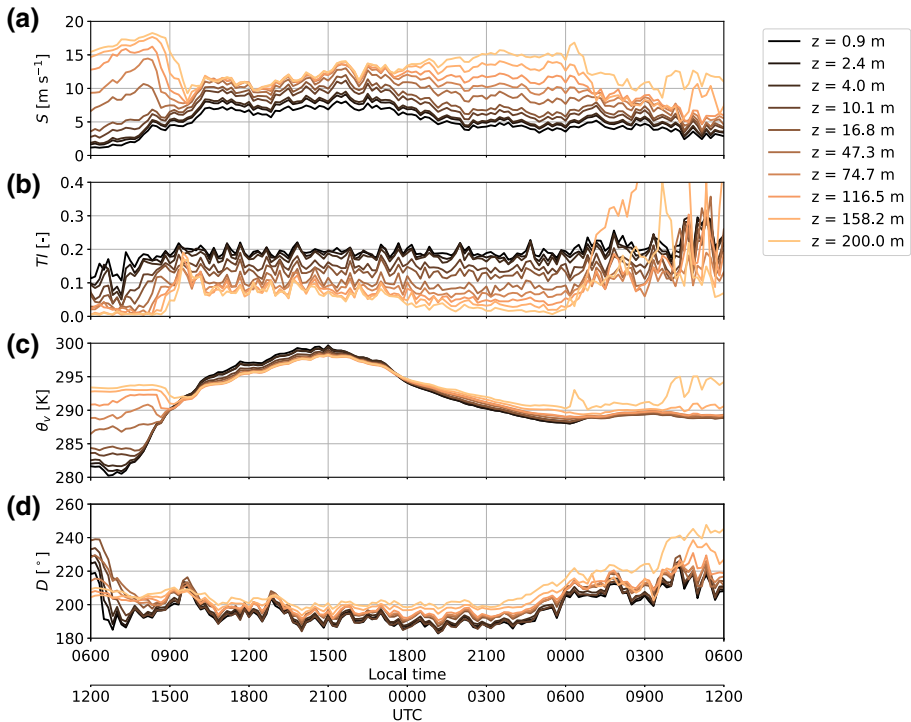
Fig. 2 Time history of the **a** wind speed S, **b** 10-min averaged turbulence intensity TI, **c** virtual potential temperature θ_v, and **d** wind direction D as measured at the TTU tower at various heights in the period 8–9 November 2013

Within the Department of Energy's Atmosphere to Electrons MMC project, meteorological conditions at the SWiFT site for the period 23 June 2012 to 31 December 2014 were analyzed to identify a quiescent diurnal cycle. The data were first searched for a consistent 1-h, near-neutral atmospheric stability condition, and subsequently filtered, requiring that the surrounding 24 h have fairly consistent wind speed and direction to remove cases with significant frontal passages. From the 36 days that satisfied this set of filter conditions, the evening transition on 8 November 2013 was selected because of its quiescent weather conditions (no precipitation or frontal passages) and typical diurnal cycle of wind speed, turbulence intensity, virtual potential temperature, and wind direction, including morning and evening transitions (Fig. 2). An LLJ develops during the night with southern wind directions throughout the simulation period, which ensures the consistent atmospheric flow conditions that are ideal for testing MMC methods. Details of the case-selection procedure and a description of the meteorological conditions during the 8 November 2013 quiescent diurnal cycle are given in Haupt et al. (2017).

Numerical results obtained with the mesoscale-to-microscale model are compared with observations from the TTU 200-m-tall meteorological tower (Kelley and Ennis 2016; Atmosphere to Electrons 2014b). The tower has vertical stations at 0.9 m, 2.4 m, 4 m, 10.1 m, 16.8 m, 47.3 m, 74.7 m, 116.5 m, 158.2 m, and 200 m, providing three-dimensional sonic anemometer velocity, temperature, barometric pressure, and relative humidity measurements. The three-dimensional propeller anemometer measurements are available at all but the low-
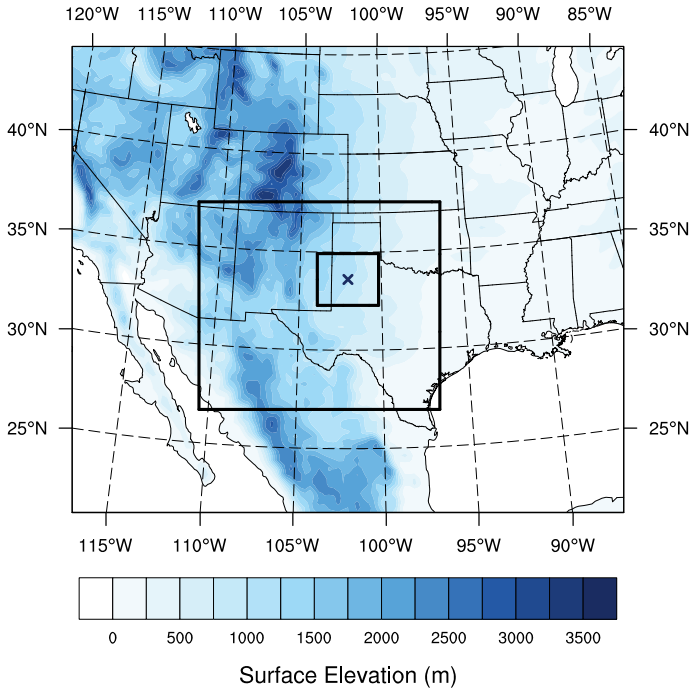
Fig. 3 Domain configuration and terrain elevation of the WRF model set-up with the state borders of the U.S.A. indicated as the black lines. The bold black rectangles indicate boundaries of the two nested domains. The cross denotes the location of the SWiFT Facility

est two stations. The sonic anemometers provide turbulence quantification as well. Raw data from the 200-m tower are recorded at a sample rate of 50 Hz.

In addition to the 200-m meteorological tower, numerical results are also compared to a Vaisala LAP-3000 wind-profiling radar (Atmosphere to Electrons 2014a), deployed by TTU about 0.5 km from the tower. The data recorded during the period of interest include two scan types: a low-range scan ("type 0," ranging from 151–1744 m above ground level, a.g.l.) and a high-range scan ("type 1," 611–6186 m a.g.l.). Thirty range gates provide 55-m and 192-m vertical resolutions for the two scans. The low-range scans had a pulse width of 400 ns and a consensus averaging time of 16 min, whereas the high-range scans had a pulse width and consensus averaging time of 2800 ns and 15 min, respectively; data were averaged in 20-min intervals.

2.2 Mesoscale Model

Mesoscale flow fields were simulated using the National Center for Atmospheric Research's Weather Research and Forecasting (WRF) model (Advanced Research WRF, version 3.7.1; Skamarock et al. 2008). The WRF model uses finite differencing to solve the compressible Euler equations, using a split time-stepping algorithm within the Runge–Kutta time-integration scheme. In the WRF model, turbulent motions of the ABL are parametrized using a boundary-layer scheme.

The WRF model simulations were initialized on 8 November 2013, at 0000 UTC to run for 48 h. The first 12 h were discarded for input in the microscale to allow for model spin-up. The

outermost domain has a 27-km grid spacing and was nested down through 9 km to an inner domain with a 3-km grid spacing (Fig. 3) and a size of $354 \times 300 \, \text{km}^2$. The timestep was set to 15 s with model output saved every 10 min of model time. We used 88 model levels spaced 5 m apart in the lowest 20 m and stretched continuously beyond that. The model was initialized and forced at the boundaries by $1° \times 1°$ United States National Center for Environmental Prediction Global Forecast System analysis at 6-h intervals. Land-use categories are sourced from the United States Geological Service (National Center for Atmospheric Research 2020). The physics and dynamics options used include the Mellor–Yamada Nakanishi and Niino (MYNN) level-2.5 boundary-layer and surface-layer (Nakanishi and Niino 2009) schemes, the unified Noah land-surface model (Tewari et al. 2004), the Rapid Radiative Transfer Model for General Circulation Models (Iacono et al. 2008), the Morrison two-moment microphysics scheme (Morrison et al. 2009), and the upper-level Rayleigh damping applied to the vertical velocity component. The turbulence and mixing options are set to evaluate second-order diffusion terms on coordinate surfaces, including the horizontal Smagorinsky first-order closure for eddy coefficient, the sixth-order up-gradient-prohibiting diffusion, the positive-definite advection option for moisture, turbulence kinetic energy (TKE, e), and scalars, the fifth-order horizontal advection for momentum and scalar, and the third-order vertical advection for momentum. Information about these options can be found in Wang et al. (2017).

2.3 Microscale Model

Microscale simulations are performed using the National Renewable Energy Laboratory's incompressible LES code, SOWFA (Simulator fOr Wind Farm Applications; see, e.g., Churchfield et al. 2012a, b), which is built upon the OpenFOAM computational fluid dynamics toolbox (The OpenFOAM Foundation 2020). The transport equations for momentum and potential temperature are discretized using an unstructured, finite-volume formulation. Advective and diffusive terms are computed using second-order central differencing (linear interpolation of quantities to cell faces), and time advancement is based on second-order backwards differencing. All variables are located at cell centres, and velocity–pressure decoupling is avoided by means of Rhie–Chow-like interpolation (Rhie and Chow 1983) of the momentum flux to cell faces. The algorithm used to solve the system of governing equations is the predictor-corrector pressure-implicit splitting operation (Issa 1985; Issa et al. 1986) with three corrector steps.

The microscale numerical domain has a size of $5 \times 5 \, \text{km}^2$ in the horizontal and 2 km in the vertical; a uniform hexahedral mesh with 10-m grid spacing in each direction is used throughout the domain. The effect of subgrid-scale motions on the resolved flow is calculated using a prognostic subgrid-scale TKE model (Deardorff 1980), and buoyancy is accounted for via the Boussinesq approximation. The microscale simulations were initialized on 8 November 2013, at 1200 UTC using WRF model profiles, and the simulations advanced for 24 h with a timestep of 0.5 s. Surface shear stress is computed using Schumann's wall model (Schumann 1975) with the aerodynamic roughness length $z_0 = 0.1$ m. The surface potential temperature is taken from WRF model data, and the surface heat flux is computed using the algorithm of Basu et al. (2008a). At the top, a slip boundary condition is used for the velocity, and the gradient of the potential temperature is set to match that of the WRF model profile used for initialization. Periodic boundary conditions are used in the horizontal directions. Finally, the latitude is set to $33.61°$ N, corresponding to the SWiFT site, and the reference potential temperature $\theta_0 = 300$ K.

2.4 Mesoscale-to-Microscale Coupling Methodology

Most microscale ABL simulations solve the following incompressible governing equations for momentum and virtual potential temperature

$$\frac{\partial \bar{u}_i}{\partial t} + \frac{\partial}{\partial x_j} \left(\bar{u}_i \bar{u}_j \right) + 2\epsilon_{ijk}\Omega_j \left(\bar{u}_k - u_k^G \right) = -\frac{1}{\rho_0}\frac{\partial \bar{p}'}{\partial x_i} - \frac{\partial \tau_{ij}^D}{x_j} + \left(\frac{\bar{\theta} - \theta_0}{\theta_0} \right) g_i, \quad (1a)$$

$$\frac{\partial \bar{\theta}}{\partial t} + \frac{\partial}{\partial x_j} \left(\bar{u}_j \bar{\theta} \right) = -\frac{\partial q_j}{\partial x_j}, \quad (1b)$$

where $\bar{u}_i$ is the resolved-scale velocity vector, ϵ_{ijk} is the alternating tensor used to indicate a cross product, Ω_j is the planetary rotation rate vector, u_k^G is the geostrophic velocity vector, ρ_0 is the constant density, $\bar{p}'$ is the resolved-scale pressure perturbation relative to: a reference value at a reference height, the hydrostatic variation with height (defined as $\rho_0 g_i x_i$), and the background mean horizontal gradient in pressure; τ_{ij}^D is the deviatoric part of the subgrid-scale stress tensor; $\bar{\theta}$ and θ_0 are the resolved-scale and reference virtual potential temperatures, respectively, which along with the gravity acceleration vector, g_i, comprise the Boussinesq buoyancy term; and q_j is the subgrid-scale temperature flux vector.

Here, we couple the microscale with the mesoscale by including realistic mesoscale forcing terms in the microscale equations, following Baas et al. (2010) and Sanz Rodrigo et al. (2017b). The microscale governing equations in Eq. 1 then become

$$\frac{\partial \bar{u}_i}{\partial t} + \frac{\partial}{\partial x_j} \left(\bar{u}_i \bar{u}_j \right) + 2\epsilon_{ijk}\Omega_j \bar{u}_k$$

$$= S_{pg,i} + S_{adv,u_i} - \frac{1}{\rho_0}\frac{\partial \bar{p}'}{\partial x_i} - \frac{\partial \tau_{ij}^D}{x_j} + \left(\frac{\bar{\theta} - \theta_0}{\theta_0} \right) g_i, \quad (2a)$$

$$\frac{\partial \bar{\theta}}{\partial t} + \frac{\partial}{\partial x_j} \left(\bar{u}_j \bar{\theta} \right) = S_{adv,\theta} - \frac{\partial q_j}{\partial x_j}, \quad (2b)$$

where the S terms are time–height-varying synoptic source terms from the mesoscale transport equation budget components that cannot naturally occur in the limited domain of the microscale simulation. Namely, $S_{pg,i}$ is the large-scale driving pressure gradient, S_{adv,u_i} is the large-scale momentum advection term, and $S_{adv,\theta}$ is the large-scale virtual potential temperature advection term.

In contrast to the microscale equations describing dry, incompressible flow that our solver uses, the mesoscale governing equations often describe compressible and moist flow, but they can be cast in the form

$$\frac{\partial U_i}{\partial t} = -\frac{\partial}{\partial x_j} \left(U_i U_j \right) - \frac{1}{\rho}\frac{\partial P}{\partial x} + F_{U_i}, \quad (3a)$$

$$\underset{\text{I}}{\frac{\partial \Theta}{\partial t}} = \underset{\text{II}}{-\frac{\partial}{\partial x_j} \left(\Theta U_j \right)} \qquad \underset{\text{III}}{} + \underset{\text{IV}}{F_\Theta}, \quad (3b)$$

where U_i, Θ, and P are the mesoscale velocity vector, virtual potential temperature, and pressure, respectively, and ρ is the local density. Here, F_{U_i} and F_Θ are any additional forcing terms arising from turbulent mixing, planetary rotation, spherical projection, and other model physics. Turbulent mixing and planetary rotation are explicitly accounted for in the microscale model.

The coupling is completed, following Lehner (2012), by including the mesoscale terms from Eq. 3 into Eq. 2 by

$$S_{pg,i} = -\frac{1}{\rho}\frac{\partial P}{\partial x_i}, \tag{4a}$$

$$S_{adv,u_i} = -\frac{\partial}{\partial x_j}\left(U_i U_j\right), \tag{4b}$$

$$S_{adv,\theta} = -\frac{\partial}{\partial x_j}\left(\Theta U_j\right). \tag{4c}$$

We acknowledge that the mesoscale pressure-gradient term $S_{pg,i}$ is scaled by the locally-varying density from the compressible mesoscale model, whereas the microscale model is incompressible and hence has a constant density. How to more rigorously address this mismatch should be the subject of future work. Additionally, surface forcing for the potential temperature equation is applied in the form of a surface skin temperature derived from the WRF model. Note that nudging towards mesoscale data or observations from a meteorological mast are not used here.

There is nothing about this coupling method that limits one to applying it to only momentum and potential temperature. Future research could explore extracting mesoscale advective terms for quantities such as moisture, and applying them to the corresponding terms within the microscale solver.

As the baseline MMC configuration, we consider a microscale simulation driven by budget components extracted from the WRF model column closest to the SWiFT site, using the 10-min output data. In this configuration, no temporal averaging is applied to the budget components, and the effective spatial averaging corresponds to the horizontal area covered by the WRF model column, which is 3×3 km^2. Further, the impact of spatial and temporal averaging is investigated based on a set of 12 simulations. We conducted spatial averaging over one 3×3-km^2 grid cell, three 3×3-km^2 grid cells (i.e., 9×9 km^2), and nine 3×3-km^2 grid cells (i.e., 27×27 km^2); temporal averaging was done over 60 min, 120 min, and 180 min. These averaging scales represent the usual grid spacing, model output frequency, and that suggested previously (Sanz Rodrigo et al. 2017b; Heinze et al. 2017). The various simulations and corresponding spatial- and temporal-averaging windows are summarized in Table 1.

3 Mesoscale-to-Microscale Simulation Results

3.1 Mesoscale Budget Components

As mentioned in Sect. 2, we extracted mesoscale budget components from the WRF model at the SWiFT facility on 8 November 2013, to couple to microscale simulations over a diurnal cycle (Fig. 2). In this section, we analyze the budget components from that day.

Figure 4 shows time–height plots of the wind speed, wind-speed tendency S_{tend} (term I in Eq. 3a), and the mesoscale budget components: the magnitude of the pressure gradient force S_{pg} (term III), advection S_{adv} (term II), Coriolis force S_{cor}, and effects from the ABL scheme S_{pbl} (Term IV). Note that for better visual representation in m s^{-1}, the components were divided by the Coriolis parameter. Figure 4 shows the lowest 2 km over 48 h using WRF model output every 10 min. The typical diurnal pattern of the ABL is clearly visible on each day. The development of a LLJ each evening is discernible through wind-speed

Table 1 Conducted coupled simulations using various averaging windows

Simulation	Averaged grid cells	Effective spatial average (km^2)	Averaging period (min)
L3_T0	1×1	3×3	None
L3_T60	1×1	3×3	60
L3_T120	1×1	3×3	120
L3_T180	1×1	3×3	180
L9_T0	3×3	9×9	None
L9_T60	3×3	9×9	60
L9_T120	3×3	9×9	120
L9_T180	3×3	9×9	180
L27_T0	9×9	27×27	None
L27_T60	9×9	27×27	60
L27_T120	9×9	27×27	120
L27_T180	9×9	27×27	180
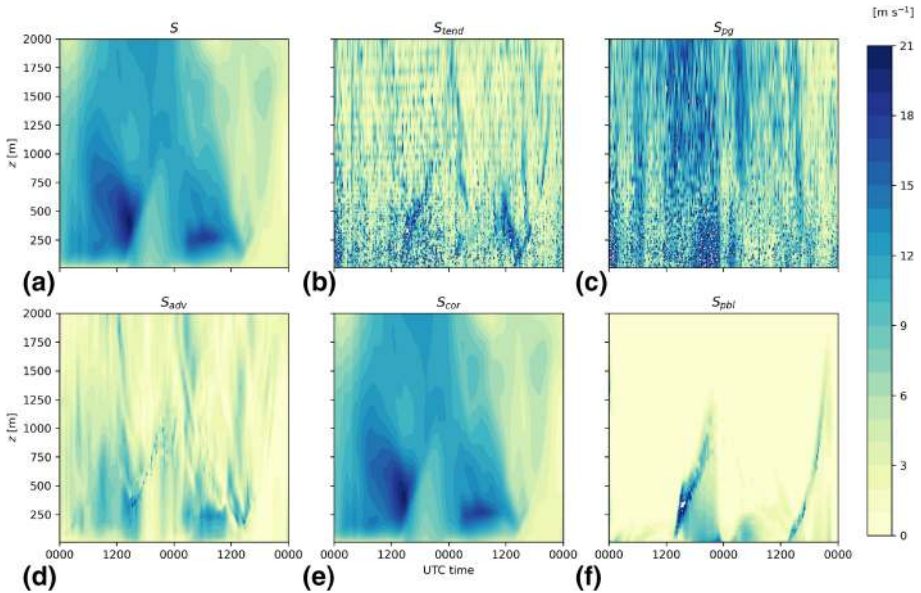
Fig. 4 Time–height plots of horizontal quantities of the momentum-budget terms presented in Eq. 3a, b: **a** wind speed S, **b** momentum budget S_{tend}, **c** pressure gradient force S_{pg}, **d** advection S_{adv}, **e** Coriolis force S_{cor}, and **f** effects from the subgrid scale S_{pbl} from 8 November 2013, 0000 UTC, to 10 November 2013, 0000 UTC, taken from the closest grid point to the SWiFT site. The budget components were divided by the Coriolis coefficient to show m s^{-1}

maxima (dark blue) in the lower third of the top left panel, as are the nontrivial magnitudes of synoptic-scale advective, pressure, and Coriolis tendencies that play strong roles in the LLJ evolution. Small-scale spatio-temporal variability is especially discernible in the terms S_{pg}, S_{adv}, and the sum of all the budget components, S_{tend}.

The evolution of the potential temperature across two diurnal cycles is shown in Fig. 5a, illustrating that the ABL starts to grow at around 1500 UTC on both days, and decreases as
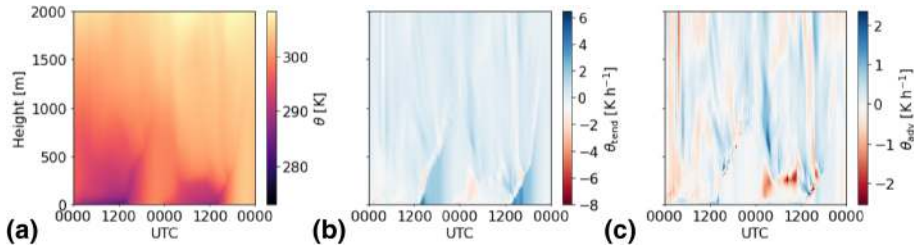
Fig. 5 Time–height plots of **a** potential temperature, **b** potential temperature tendency (term I in Eq. 3b), and **c** potential temperature advection (term II) in K h^{-1} from 8 November 0000 UTC to 10 November 0000 UTC, taken from the closest grid point to the SWiFT site
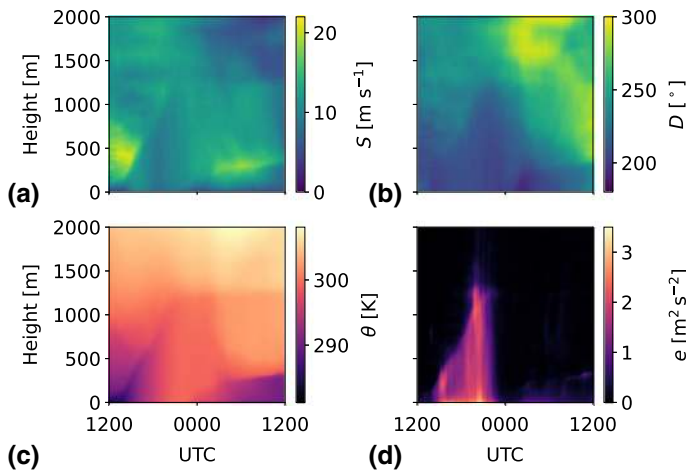

Fig. 6 Time–height plots of microscale simulation results for **a** wind speed, **b** wind direction, **c** potential temperature, and **d** resolved TKE from 8 November 1200 UTC until 9 November 2013 1200 UTC. The results correspond to simulation L3_T0 and have been averaged over horizontal planes

it returns to atmospheric stable conditions during the night. The top of the ABL is especially visible in the temperature tendency (b) as well as in Fig. 6, showing microscale simulation results. The importance of the advective component of the temperature tendency, especially on the second simulated day, is shown by much more pronounced magnitudes than on the first day (high values around 300 m a.g.l.). We therefore conclude that temperature advection is an important contributor to the atmospheric stability in the ABL on that day.

3.2 Microscale Flow Results

In this section, we evaluate the microscale LES results driven by the mesoscale budget components discussed in the previous section. We first consider the general flow behaviour in terms of the wind speed and direction, potential temperature, and TKE in Fig. 6. Note that the microscale results are only shown for one day.

We find that the main temporal evolution of the microscale prediction of mean-flow quantities follows the larger-scale diurnal patterns that were observed previously in the mesoscale output, including the diurnal growth and collapse of the ABL and the development of a

nocturnal LLJ. Further, the time–height plot of TKE shows that the intensity of the resolved turbulence complies with the mean-flow dynamics, exhibiting high levels in the daytime convective boundary layer and a subsequent decay to low-level turbulence at night. Next, Fig. 7 depicts the time history of the same quantities at a typical turbine-hub height of 80 m and enables a qualitative comparison between mesoscale and microscale results and TTU tower observations. During the daytime, the wind speed predicted by the microscale model is sometimes up to about 2 m s^{-1} higher than the results from the mesoscale simulation, and at night differences in the wind direction of $\approx 10°$ are observed. In general, however, trends in the microscale results closely follow the mesoscale data both in terms of the velocity and potential temperature. Consequently, the agreement between the mesoscale-to-microscale prediction and the observations in terms of these mean-flow quantities depends to a large extent on the accuracy of the mesoscale simulation. For example, the large oscillation in observed wind speed between 1200 and 1600 UTC is captured by neither the mesoscale nor the microscale model, and both solvers' prediction of a potential temperature decrease associated with the development of the night-time stable boundary layer appears to lag several hours behind the TTU tower observations.

We evaluate the time history of the TKE in Fig. 7d. Here, the TKE from the LES model is evaluated from planar averages to be consistent with the WRF model simulations, which can also be thought of as planar averages. Since the forcing for the LES model originates from the WRF model, we chose to evaluate planar averages, even though the observations are point measurements. In Fig. 7d, the microscale results agree well with the observations, capturing both the high levels of turbulence during the daytime (overpredicted) and the low variability during the night. Moreover, the timing of the evening transition and decay of turbulence are predicted relatively well, especially when comparing with the timing of the potential temperature decrease in Fig. 7c. Finally, we observe that, from the start of the simulation, the TKE increases immediately, which seems to suggest a rapid spin-up of turbulence. After 1 h, the entire numerical domain is filled with adequate turbulent structures (not shown) which are continuously recycled by the periodic lateral boundary conditions.

Consider the vertical structure of the ABL in Fig. 8 where the vertical profiles are averaged over 1 h at 1800 UTC, 2200 UTC, and 0600 UTC, corresponding to convective, neutral, and stable conditions at 1200 LT (local time = UTC − 6 h), 1600 LT, and 0000 LT, respectively. The wind-speed profile representing convective conditions in Fig. 8a shows that the mesoscale simulation underpredicts the wind speed when compared with the observations, and the microscale simulation is not able to correct this mean bias. However, the high wind shear in the mesoscale profile, as produced by the MYNN ABL scheme, is modified by the resolved turbulent structures in the microscale simulation, leading to a more uniform wind speed between the surface layer and the top of the convective boundary layer (Fig. 8). A similar effect is observed in the potential-temperature profile in Fig. 8c, where the superadiabatic mesoscale profile is modified by resolved turbulence in the microscale to yield a more well-mixed profile. Again, the superadiabatic mesoscale profile is likely due to using a local solver such as the MYNN ABL parametrization. Finally, the resolved TKE during convective conditions in Fig. 8d is higher than the observed values of TKE, but the decrease of TKE with height is well predicted.

The vertical profiles for near-neutral conditions in Fig. 8e–h show that the mesoscale biases in the wind speed and direction, and potential-temperature are not corrected by the microscale simulation, but the wind shear and potential-temperature gradient are more uniform throughout the boundary layer. Moreover, we observe that the microscale boundary-layer height (indicated by, for example, jumps in the wind speed and direction and potential temperature, and a sudden decrease of the TKE with height) in both convective and neutral conditions is
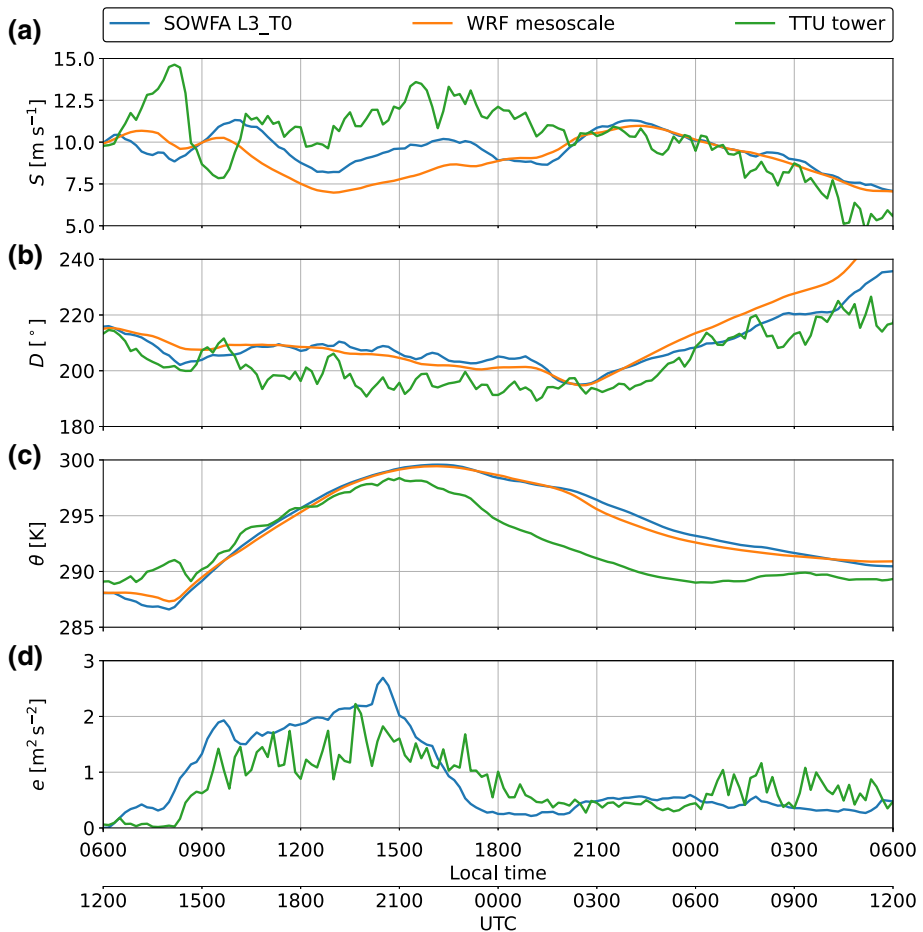
Fig. 7 Time history at a height of 80 m of the **a** wind speed, **b** wind direction, **c** potential temperature, and **d** TKE, e, comparing microscale results of simulation L3_T0 with WRF model mesoscale results and observations from the TTU tower from 8 November 1200 UTC until 9 November 2013 1200 UTC. The microscale results have been averaged over horizontal planes

higher than that predicted by the WRF model, which indicates a higher level of turbulent mixing in the microscale simulation. Figure 8h shows that the microscale near-neutral TKE profile matches well with the observations.

For stable conditions (Fig. 8i–l), the mesoscale model reproduces well the LLJ wind speed, and the same is true for the microscale result. Between 750 and 1250 m, the wind speed profile computed from microscale model simulation deviates from the mesoscale results and field measurements, which we hypothesize is due to the simulated TKE being too high during the day, which continues into the residual layer at night. Future work could also explore whether this deviation is caused by the negative wind shear, as suggested by a step change in TKE between 500 and 750 m (Fig. 8l). Note that the approach of using mesoscale budget components to drive the microscale simulation can make the microscale solution diverge from the mesoscale input as this method only provides external forcing. The mesoscale potential temperature is too high compared with the observations, and, therefore, so is the
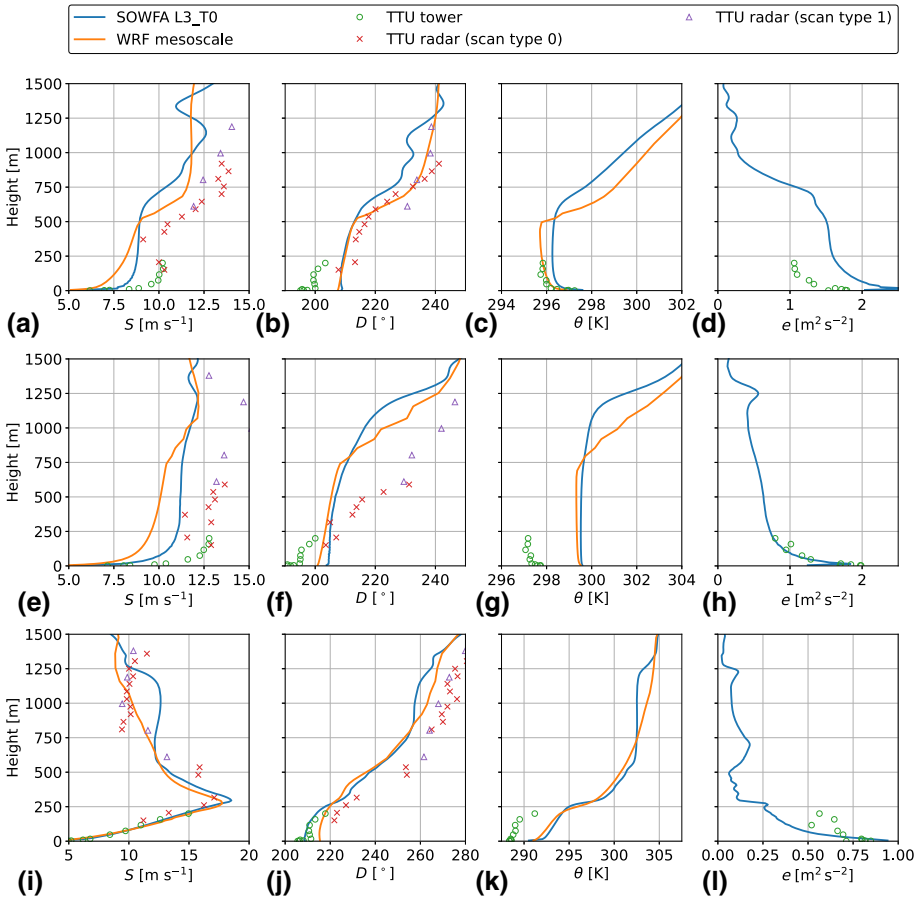
Fig. 8 Vertical profiles of **a**, **e**, **i** wind speed, **b**, **f**, **j** wind direction, **c**, **g**, **k** virtual potential temperature, and **d**, **h**, **l** TKE, averaged over 1 h starting at **a–d** 1800 UTC on 8 November 2013, **e–h** 2200 UTC on 8 November 2013, and **i–l** 0600 UTC on 9 November 2013. Planar-averaged microscale results of simulation L3_T0 are compared with the WRF mesoscale results and observations from the TTU tower

microscale potential temperature. In terms of the TKE, the microscale result agrees well with the observations.

The distribution of TKE across structures of different scales is illustrated in Fig. 9 by means of the power spectral density of the streamwise and vertical velocity components and potential temperature fluctuations. The temporal spectra are calculated for 1 h of data starting at 1800 UTC (convective), 2200 UTC (neutral), and 0600 UTC (stable), using Welch's method (Welch 1967) with 10-min segments, 50% overlap, and a Hann window function (Harris 1978). It is shown that, given information about the mesoscale flow, the microscale solver is able to contribute smaller-scale turbulent structures resulting from the mesoscale internal and surface forcing. Compared with the turbulence spectra observed at the TTU tower, there is an overestimation of turbulence energy at higher frequencies close to the cut-off frequency in Fig. 9a, and there are also noticeable differences in Fig. 9c, f, and i for stable conditions, which are typically more difficult to capture with the LES approach. We also see a sharper roll-off (i.e., slope changes) of energy in the simulations than in the
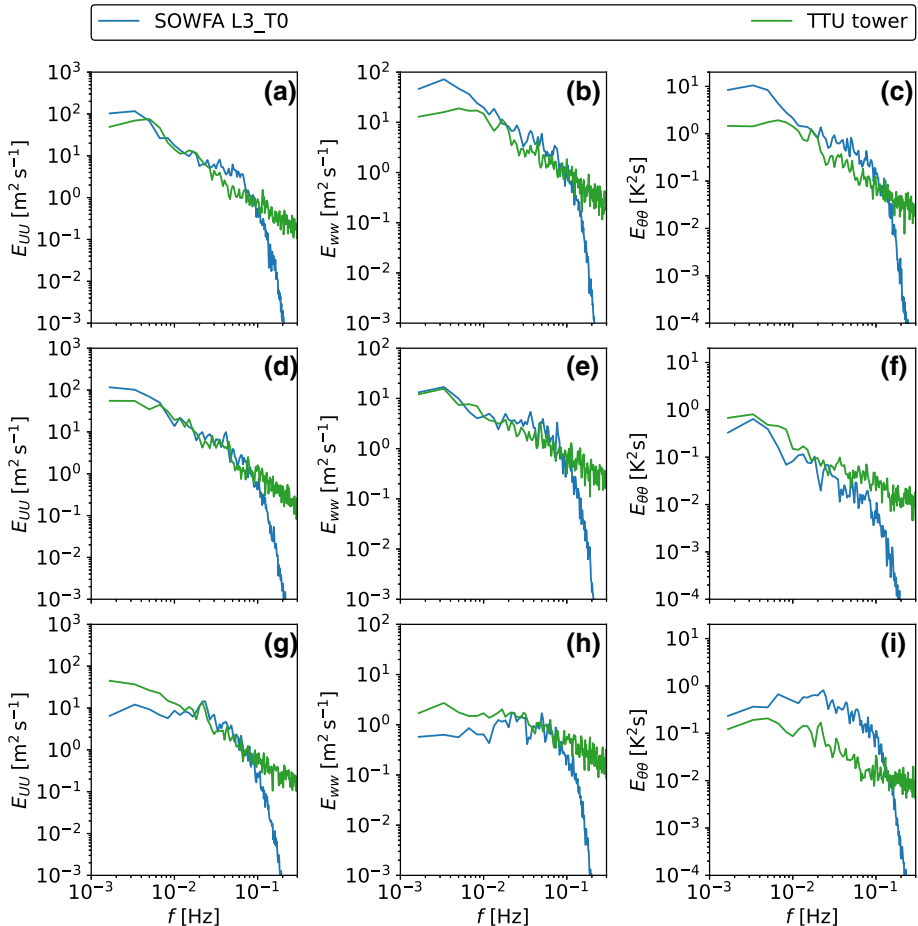
Fig. 9 Power spectral density of turbulent fluctuations in **a**, **d**, **g** the streamwise velocity component, **b**, **e**, **h** vertical velocity component, and **c**, **f**, **i** potential temperature at 80 m using 1 h of data starting at **a–c** 1800 UTC on 8 November 2013, (d–f) 2200 UTC on 8 November 2013, and **g–i** 0600 UTC on 9 November 2013. Microscale spectra corresponding to simulation L3_T0 are compared with observations from the TTU tower

observations. Furthermore, the low-frequency content of turbulence depends on the time of the day. The low-frequency signal in the microscale could be related to the mesoscale forcing passed to the microscale solver. There does not seem to be a pattern discernible with regard to spectral differences between observations and simulations. Future work could explore whether a finer grid spacing would reduce the spectral differences between observations and simulations during stable conditions.

4 Impact of Spatial and Temporal Averaging

4.1 Mesoscale Input to the Microscale

We now evaluate the effect of spatial and temporal averaging on the mesoscale budget components, since the need for averaging has been emphasized previously (Heinze et al. 2017;
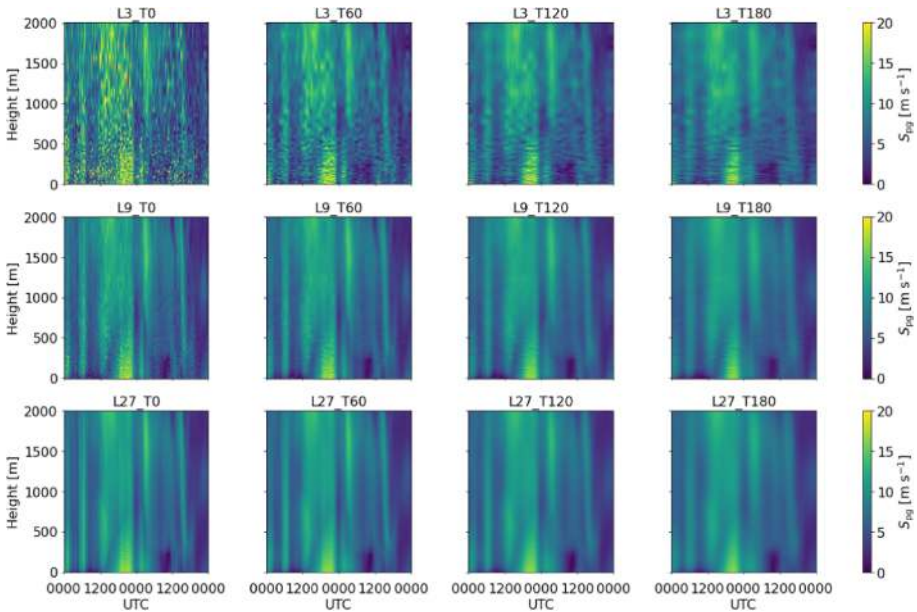
Fig. 10 Time–height plots of S_{pg} over 48 h for all the experiments listed in Table 1

Arroyo et al. 2018; Olsen 2018). Arroyo et al. (2018) found that, for their case in complex terrain, the pressure-gradient forcing S_{pg} (term III in Eq. 3a) is particularly noisy for their 3-km grid (which agrees with our findings), stating that the pressure gradient accounts also for small-scale advection generated by the terrain at that scale, and concluding that small-scale advection should be accounted for by the microscale model. Here and in the next section, we analyze the momentum budget components to deduce whether averaging or smoothing of the budget components is necessary for successful implementation of the MMC approach.

The advective component of the momentum tendency S_{adv} and the component describing the pressure gradient S_{pg} exhibit the most spatio-temporal variability (Fig. 4), and as these are the two components coupled to the microscale, we investigate them here in more detail. Figure 10 shows time–height plots over 48 h of the term S_{pg} for all 12 conducted experiments (Table 1), sorted into rows for spatial averaging and columns for temporal averaging, illustrating that the variability clearly reduces from the top left to the bottom right. This shows that averaging instantaneous output may be advantageous in reducing noise, yet averaging over too big an area (e.g., 27 km) and too long a period (e.g., 3 h) does not change the budget components considerably in this case. Moreover, large averaging periods and areas may have disadvantages because the signals in the data are too smooth, or features over too long a distance are averaged together and hide the mesoscale feature of interest (e.g., the timing and location of a front would be wrong). Lastly, Fig. 10 shows that spatial averaging is more effective than temporal averaging in decreasing the variability, with the same conclusions also holding for the advective term S_{adv} (not shown).

Spectra of the terms S_{pg} and S_{adv} for all cases are shown in Fig. 11. In general, the longer the temporal average and the larger the area over which the budget components are averaged, the more energy is reduced, which is consistent with Fig. 10. It is apparent that the differences between the cases are only pronounced at higher frequencies. The reduction of energy for 1-h temporal averages occurs at higher frequencies than for the 2- and 3-h temporal averages
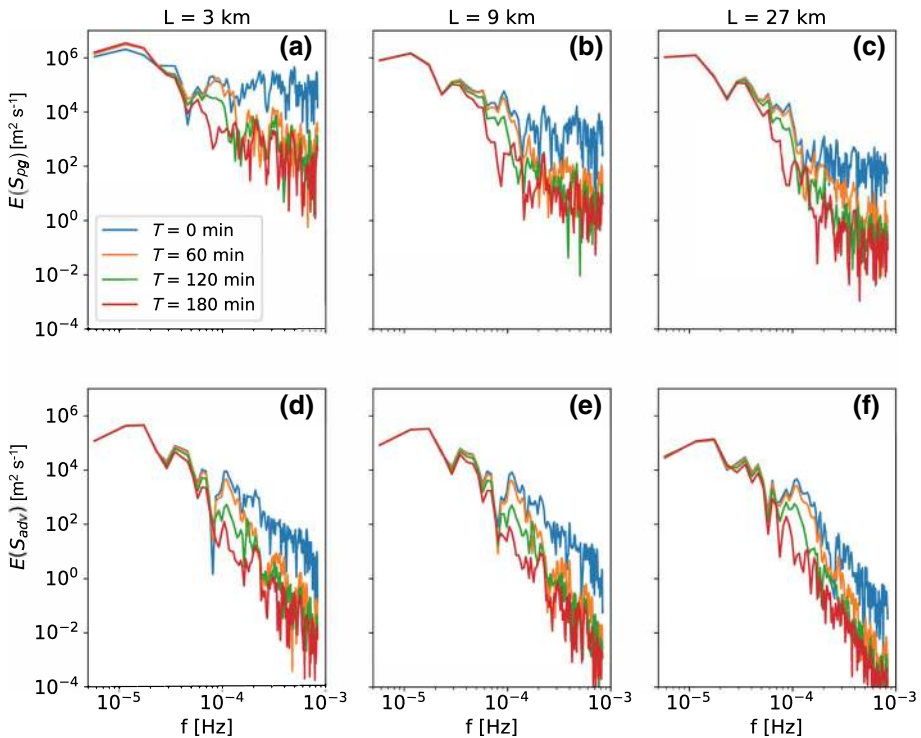
Fig. 11 Power spectral density of **a–c** the pressure-gradient tendency S_{pg} and **d–f** the advective component of the momentum tendency S_{adv}, extracted from the WRF model at the closest grid point to the SWiFT site at 80 m. The spectra are computed over 48 h for spatially-averaged WRF model output over a (left column) 3×3 km^2, (middle column) 9×9 km^2, and (right column) 27×27 km^2 set of grid cells for the various averaging times T0/60/120/180 min

(i.e., the orange line for $T = 60$ min falls off later than the lines for $T = 120$ min and $T = 180$ min, which is to be expected). We also find that the spectra of the term S_{adv} fall off faster than for the term S_{pg}.

Assuming a mean wind speed at 80 m of approximately 10 m s^{-1} (Fig. 7), a temporal average of 1 h corresponds to a spatial average of 36 km using Taylor's frozen turbulence hypothesis. Therefore, and because the energy is reduced more for the 9-km and 27-km spatial averages with 1-h temporal averaging (Fig. 11b, c, e, f), as opposed to 2-h and 3-h temporal averages with 3-km spatial averaging (Fig. 11a, d), we conclude that spatial averages are more effective in reducing noise than temporal averages. However, averaging over too large an area (e.g., 27 km) may be disadvantageous in capturing desired mesoscale features.

4.2 Impact on the Microscale

The impact of spatially and/or temporally averaging the mesoscale budget components on the microscale simulation results is illustrated in Fig. 12, which shows time–height plots of wind speed for all experiments listed in Table 1.

We find that, also in the microscale, the spatio-temporal variability decreases with an increasing spatial- and temporal-averaging window of the mesoscale budget components.
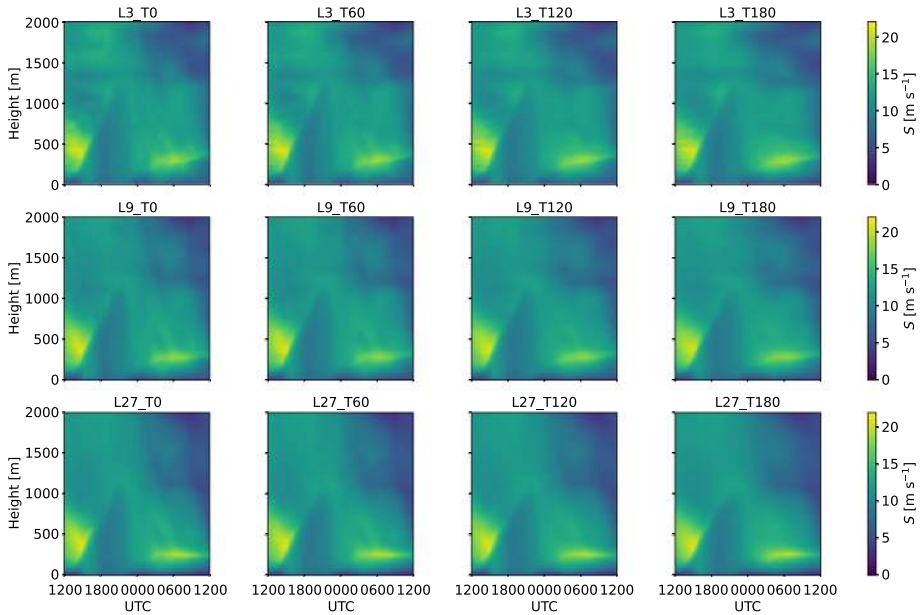
Fig. 12 Time–height plots of microscale wind speed from 8 November 1200 UTC until 9 November 2013 1200 UTC for all the experiments listed in Table 1. The microscale results have been averaged over horizontal planes

However, the main flow features and ABL dynamics are similar among the different simulations and do not seem to depend much on the degree of averaging. The same conclusion holds for other microscale quantities such as the wind direction, potential temperature, and TKE (not shown).

To further quantify the impact on microscale results of spatially and/or temporally averaging the mesoscale budget components, we evaluate the error between simulated and observed quantities of interest in Fig. 13.

We consider the wind speed and direction, potential temperature, wind shear and wind veer, TKE, and turbulence intensity, averaged across a reference rotor span between 40 and 200 m (characteristic of an 8-MW large wind turbine). Following Sanz Rodrigo et al. (2017b), the wind shear α is estimated by fitting a power-law to the planar-averaged wind speed at all simulated heights within the rotor region. Similarly, the wind veer Ψ is calculated by a linear curve fit to the planar-averaged wind direction. The mean and standard deviation of the error are calculated for 1 h of data starting at 1800 UTC (convective), 2200 UTC (neutral), and 0600 UTC (stable conditions).

For most of the wind-energy quantities of interest in Fig. 13, we find that the mean error with respect to the TTU tower observations is very similar among the various simulations, especially when the stability conditions are convective (1800 UTC) or neutral (2200 UTC). During stable conditions (0600 UTC), we find that averaging of mesoscale budget components has an impact on certain variables. For example, using a large spatial averaging window of 27×27 km^2 (simulations L27_T0/60/120/180, represented in red) leads to greater errors in terms of the wind speed and direction. Interestingly, the microscale simulations show a reduced error compared with the WRF model simulations for the wind speed for convective and neutral conditions, but show a similar error for stable conditions, indicating that the
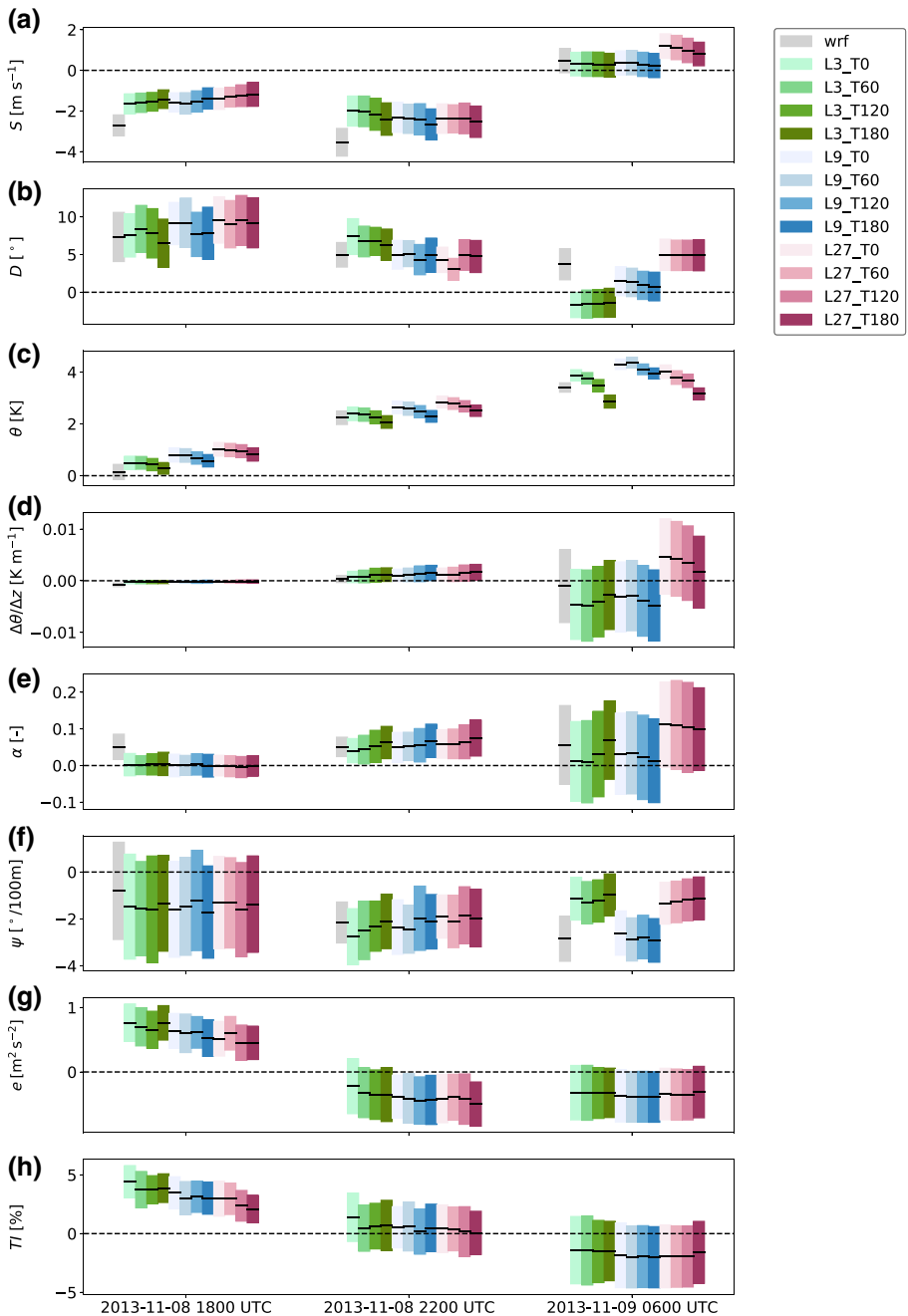
Fig. 13 Error between simulations and TTU tower observations, in terms of various quantities of interest averaged across a reference rotor span between 40 and 200 m: **a** wind speed, **b** wind direction, **c** potential temperature, **d** potential temperature gradient across rotor span, **e** wind shear, **f** wind veer, **g** TKE, and **h** turbulence intensity. Every simulation is represented by a coloured bar centred at the mean error (black line) with a height equal to twice the standard deviation. The mean and standard deviation of the error are calculated based on 1 h of data starting at 1800 UTC, 2200 UTC, and 0600 UTC
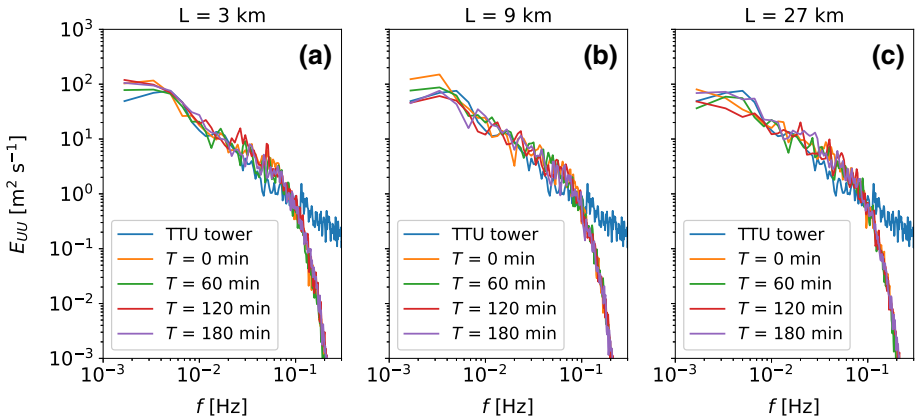
Fig. 14 Power spectral density of turbulent fluctuations in the wind speed, obtained with microscale simulations for the cases **a** L3_T0/60/120/180, **b** L9_T0/60/120/180, and **c** L27_T0/60/120/180. The microscale spectra are calculated at 80 m using 1 h of data starting at 1800 UTC, and the results are compared with observations from the TTU tower

microscale simulations are able to reduce the error from the mesoscale input with respect to the wind speed. For wind-energy applications, the accurate prediction of the wind speed is important. Equally important, though, is how well a flow model predicts the mean wind speed and potential temperature profiles. The wind shear has a significant impact on wind-turbine fatigue loading at the rotor rotation frequency, and the potential temperature gradient dictates the buoyancy production of turbulence. From Fig. 13, we see that, during convective conditions, the error in the wind speed and potential temperature gradient is reduced to nearly zero in the microscale simulation versus the WRF model results. At other times of day, an error reduction is realized as long as the area over which the spatial averaging is applied is not too large. Whether the reduction in error of the microscale predictions is a consistent trend is not completely clear because we have only simulated a single day. A multiday or full-week simulation would likely be necessary to make conclusive claims about microscale error reductions. The spatial averaging has a dramatic effect on the wind direction during stable conditions (calculated from the planar-averaged velocity components, which is also more sensitive to spatial averaging than temporal averaging, and more sensitive than any of the other quantities during any period). Furthermore, while temporal averaging seems to have the strongest impact on the potential temperature, there is not a single combination of spatial and temporal averaging that reduces the mean error significantly and consistently over different time windows for the various quantities of interest.

Finally, Fig. 14 shows that the spectra of the various microscale simulations all collapse on top of each other and that averaging of the mesoscale budget components does not impact the spectrum of the microscale turbulence. This finding also holds for other variables and at other times of the day (not shown). Therefore, we conclude that the spatio-temporal variability of the mesoscale internal forces has very little impact on the microscale results, and that averaging of mesoscale budget components is not needed when coupling with microscale LES models.

5 Conclusions

Because the MMC approach allows for a microscale LES model of a much wider variety of atmospheric conditions, we evaluate the performance of the MMC approach by applying mesoscale momentum and temperature transport equation budget terms to the microscale transport equations as time–height varying source terms. Using mesoscale budget components as input to a microscale model is one of the most straightforward ways of executing the MMC technique, which has been successfully used in a number of studies (listed in Sect. 1). We also conclude that, generally, this method of coupling performs well for the diurnal cycle at the SWiFT site test case investigated here.

We find that, as the main temporal evolution of the microscale prediction of mean-flow quantities follows larger-scale diurnal patterns of the mesoscale model output, with regard to applying LES models for the MMC technique, the accuracy of the mesoscale model output determines the accuracy of the microscale model output for the mean-flow quantities. We further observed higher levels of turbulent mixing in the microscale than in the mesoscale simulations.

For most of the wind-energy quantities of interest, the mean error with respect to the TTU tower observations is very similar among the various simulations, especially during convective or neutral stability conditions. We further show that the mesoscale bias in wind speed and direction, and potential temperature is not corrected by the microscale simulation. However, the microscale wind shear and potential temperature gradient are more uniform throughout the boundary layer, and, therefore, are corrected by the microscale model. As noted in Sect. 3.2, the vertical gradients of horizontally-averaged temperature and velocity may be attributed to the MYNN ABL parametrization used here. In general, the MMC prediction of the turbulence energy cascade agrees fairly well with the observations, even when there is a bias in the prediction of mean-flow quantities.

Generally, these findings affirm our first hypothesis:

(i) The mesoscale models have difficulties predicting profiles for shear and veer, and the LES approach can correct the mesoscale predictions for shear and veer but, as expected, cannot adjust the magnitude of the wind speed and direction.

Because it is unclear from the literature whether the spatio-temporal variability of the larger-scale budget components has an effect on the microscale, we studied how wind-energy quantities of interest computed within the microscale LES model are affected by applying different levels of variability-reducing spatial and temporal averaging of the source terms derived from mesoscale budget components.

Results show that averaging reduces the spatio-temporal variability of the momentum budget components, and that spatial averages are more effective in reducing this variability than temporal averages. This makes spatial averaging of the momentum budget components more advantageous than temporal averaging, because, apart from being more effective, it preserves time-varying features that should be passed onto the microscale. We caution that averaging over too large an area (e.g., $27 \times 27 \ km^2$) might be disadvantageous in capturing desired mesoscale features. Even though in the region of the TTU tower the terrain is relatively flat, one should not assume that the budget component fields are horizontally homogeneous. In fact, we have found them to be horizontally heterogeneous, lasting several hours (i.e., they are in quasi-equilibrium; Fig. 15). Therefore, spatial averaging about the point of interest can introduce additional budget-component effects at the point of interest, which is undesirable.
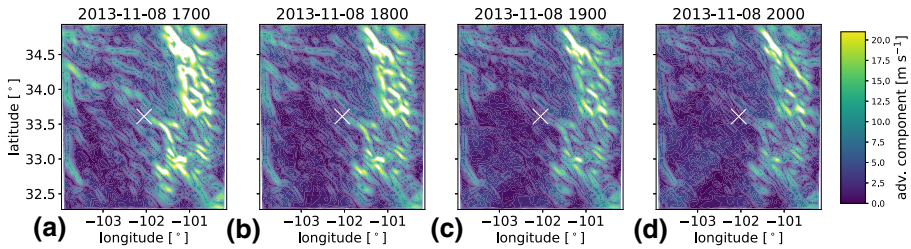
Fig. 15 Advection term of the mesoscale momentum budget, S_{adv}, across the innermost WRF modelling domain at 1700, 1800, 1900, and 2000 UTC at 117 m a.g.l. The advection budget term is divided by the Coriolis parameter to convert to the units of m s^{-1}. The cross denotes the location of the TTU tower

However, in the end, there is not a single combination of spatial and temporal averaging windows that reduces the mean error significantly and consistently over the different time windows for the various quantities of interest.

These findings concerning mesoscale budget averaging partially disprove our remaining two hypotheses in the following ways:

(ii) Although Sanz Rodrigo et al. (2017b) state that averaging effectively removes noise in the budget component time history and spatial field, we find that it is not important, or sometimes disadvantageous, for the LES approach, which is counter to our original hypothesis. It is unclear why some of the budget component fields contain seemingly unphysical noise, but we conclude that, at least in the case simulated here, the noise of the budget component field is of high enough frequency and/or small enough magnitude that it cannot effectively overcome the inertia of the mean field and the turbulence does not react fast enough to it to cause noticeable changes to turbulence properties.

(iii) If averaging must be performed, spatial averaging of budget components is more efficient than temporal averaging in that more extensive smoothing can be achieved with less data. However, if quasi-stationary spatial structures are present in the budget components, spatial averaging is not recommended. Also, by temporally averaging the budget components, we lose desired signals in certain mesoscale events (e.g., the exact timing of a cold front passage). This violates the motivation for coupling the mesoscale to the microscale, which is to integrate accurate simulations of mesoscale events into a microscale model.

In conclusion, because averaging the budget components shows no significant impact on the mean-flow quantities in the microscale, and given the effects of spatial and temporal averaging listed above, averaging is not necessary when coupling mesoscale budget components to the LES model.

The presented results apply to a quiescent diurnal cycle over flat terrain. Future studies should investigate various mesoscale phenomena, such as frontal passages, or different terrain. However, as indicated in the Introduction, the method needs to be adjusted over inhomogeneous terrain and for strong gradients in mesoscale signals. Additional studies should investigate the impact of coupling mesoscale budget components to a LES solver by analyzing the observed and simulated power predictions of wind farms, for example, by using actuator lines or disks in the LES model.

References

Allaerts D, Quon E, Draxl C, Churchfield MJ (2020) Development of a time-height profile assimilation technique for large-eddy simulation. Boundary-Layer Meteorol. https://doi.org/10.1007/s10546-020-00538-5

Arroyo RC, Indave AI, Rodrigo JS, Correia PF (2018) Analysis and validation of weather research and forecasting model tendencies for meso-to-microscale modelling of the atmospheric boundary layer. J Phys: Conf Ser 1037(072):012. https://doi.org/10.1088/1742-6596/1037/7/072012

Atmosphere to Electrons (2014a) mmc/radar.z01.00. Maintained by A2e Data Archive and Portal for U.S. Department of Energy, Office of Energy Efficiency and Renewable Energy. https://doi.org/10.21947/1329730

Atmosphere to Electrons (2014b) mmc/tower.z01.00. Maintained by A2e Data Archive and Portal for U.S. Department of Energy, Office of Energy Efficiency and Renewable Energy. https://doi.org/10.21947/1329252

Baas P, Bosveld FC, Lenderink G, van Meijgaard E, Holtslag AAM (2010) How to design single-column model experiments for comparison with observed nocturnal low-level jets. Q J R Meteorol Soc 136(648):671–684

Basu S, Holtslag AAM, Van De Wiel BJH, Moene AF, Steeneveld GJ (2008a) An inconvenient "truth" about using sensible heat flux as a surface boundary condition in models under stably stratified regimes. Acta Geophys 56(1):88–99. https://doi.org/10.2478/s11600-007-0038-y

Basu S, Vinuesa JF, Swift A (2008b) Dynamic les modeling of a diurnal cycle. J Appl Meteorol Clim 47(4):1156–1174. https://doi.org/10.1175/2007JAMC1677.1

Castro F, Silva Santos C, Lopes da Costa J (2015) One-way mesoscale-microscale coupling for the simulation of atmospheric flows over complex terrain. Wind Energy 18(7):1251–1272. https://doi.org/10.1002/we.1758

Churchfield MJ, Lee S, Michalakes J, Moriarty PJ (2012a) A numerical study of the effects of atmospheric and wake turbulence on wind turbine dynamics. J Turbul 13(14):1–32

Churchfield MJ, Lee S, Moriarty PJ, Martinez LA, Leonardi S, Vijayakumar G, Brasseur J (2012b) A large-eddy simulation of wind-plant aerodynamics. In: Proceedings of 50th AIAA Aerospace Sciences Meeting including the New Horizons Forum and Aerospace Exposition

Deardorff JW (1980) Stratocumulus-capped mixed layers derived from a three-dimensional model. Boundary-Layer Meteorol 18(4):495–527

Duynkerke PG, de Roode SR, van Zanten MC, Calvo J, Cuxart J, Cheinet S, Chlond A, Grenier H, Jonker PJ, Köhler M, Lenderink G, Lewellen D, Lappen C, Lock AP, Moeng CH, Müller F, Olmeda D, Piriou JM, Sánchez E, Sednev I (2004) Observations and numerical simulations of the diurnal cycle of the EUROCS stratocumulus case. Q J R Meteorol Soc 130(604):3269–3296. https://doi.org/10.1256/qj.03.139

Englberger A, Dörnbrack A (2018) Impact of the diurnal cycle of the atmospheric boundary layer on wind-turbine wakes: A numerical modelling study. Boundary-Layer Meteorol 166(3):423–448. https://doi.org/10.1007/s10546-017-0309-3

Gopalan H, Gundling C, Brown K, Roget B, Sitaraman J, Mirocha JD, Miller WO (2014) A coupled mesoscale-microscale framework for wind resource estimation and farm aerodynamics. J Wind Eng Ind Aerodyn 132:13–26. https://doi.org/10.1016/j.jweia.2014.06.001

Harris FJ (1978) On the use of windows for harmonic analysis with the discrete Fourier transform. In: Proceedings of IEEE, pp 51–83

Haupt SE, Anderson A, Berg L, Brown B, Churchfield M, Ennis BL, Feng Y, Kosović B, Kotamarthi R, Linn R, Mirocha JD, Moriarty P, Muñoz Esparza D, Rai R, Shaw WJ (2015) First year report of the Atmosphere to Electrons Mesoscale to Microscale Coupling Project. Pacific Northwest National Laboratory, Richland, WA, Tech Rep PNNL-25108

Haupt SE, Kotamarthi R, Feng Y, Mirocha JD, Koo E, Linn R, Kosović B, Brown B, Anderson A, Churchfield MJ, Draxl C, Quon E, Shaw W, Berg L, Rai R, Ennis BL (2017) Second year report of the Atmosphere to Electrons Mesoscale to Microscale Coupling Project: Nonstationary modeling techniques and assessment. Pacific Northwest National Laboratory, Richland, WA, Tech Rep PNNL-26267

Heinze R, Moseley C, Böske LN, Muppa SK, Maurer V, Raasch S, Stevens B (2017) Evaluation of large-eddy simulations forced with mesoscale model output for a multi-week period during a measurement campaign. Atmos Chem Phys 17(11):7083–7109

Hirth B, Schroeder J (2014) A summary of the National Wind Institute meteorological measurement facilities at the Texas Tech University's Reese Technology Center field site. Texas Tech University, Tech rep

Iacono MJ, Delamere JS, Mlawer EJ, Shephard MW, Clough SA, Collins WD (2008) Radiative forcing by long-lived greenhouse gases: calculations with the AER radiative transfer models. J Geophys Res Atmos. https://doi.org/10.1029/2008JD009944

Issa RI (1985) Solution of the implicitly discretized fluid flow equations by operator-splitting. J Comput Phys 62:40–65

Issa RI, Gosman AD, Watkins AP (1986) The computation of compressible and incompressible recirculating flow by a non-iterative implicit scheme. J Comput Phys 62:66–82

Kelley CL, Ennis BL (2016) SWiFT site atmospheric characterization. Sandia National Laboratories, Albuquerque, NM, Tech Rep SAND2016-2016

Kleissl J, Kumar V, Meneveau C, Parlange MB (2006) Numerical study of dynamic smagorinsky models in large-eddy simulation of the atmospheric boundary layer: validation in stable and unstable conditions. Water Resour Res. https://doi.org/10.1029/2005WR004685

Kumar V, Kleissl J, Meneveau C, Parlange MB (2006) Large-eddy simulation of a diurnal cycle of the atmospheric boundary layer: atmospheric stability and scaling issues. Water Resour Res 42(6):1–18

Kumar V, Svensson G, Holtslag AAM, Meneveau C, Parlange MB (2010) Impact of surface flux formulations and geostrophic forcing on large-eddy simulations of diurnal atmospheric boundary layer flow. J Appl Meteorol Clim 49(7):1496–1516. https://doi.org/10.1175/2010JAMC2145.1

Lehner M (2012) Observations and large-eddy simulations of the thermally driven cross-basin circulation in a small, close basin. PhD thesis, University of Utah

Mirocha J, Kosović B, Kirkil G (2014) Resolved turbulence characteristics in large-eddy simulations nested within mesoscale simulations using the weather research and forecasting model. Mon Weather Rev 142(2):806–831. https://doi.org/10.1175/MWR-D-13-00064.1

Mirocha JD, Lundquist JK, Kosović B (2010) Implementation of a nonlinear subfilter turbulence stress model for large-eddy simulation in the advanced research WRF model. Mon Weather Rev 138(11):4212–4228. https://doi.org/10.1175/2010MWR3286.1

Morrison H, Thompson G, Tatarskii V (2009) Impact of cloud microphysics on the development of trailing stratiform precipitation in a simulated squall line: comparison of one- and two-moment schemes. Mon Weather Rev 137(3):991–1007. https://doi.org/10.1175/2008MWR2556.1

Muñoz-Esparza D, Kosović B (2018) Generation of inflow turbulence in large-eddy simulations of nonneutral atmospheric boundary layers with the cell perturbation method. Mon Weather Rev 146(6):1889–1909. https://doi.org/10.1175/MWR-D-18-0077.1

Muñoz-Esparza D, Kosović B, Mirocha J, van Beeck J (2014) Bridging the transition from mesoscale to microscale turbulence in numerical weather prediction models. Boundary-Layer Meteorol 153(3):409–440. https://doi.org/10.1007/s10546-014-9956-9

Muñoz-Esparza D, Kosović B, van Beeck J, Mirocha J (2015) A stochastic perturbation method to generate inflow turbulence in large-eddy simulation models: application to neutrally stratified atmospheric boundary layers. Phys Fluids 27(3):035102. https://doi.org/10.1063/1.4913572

Muñoz-Esparza D, Lundquist JK, Sauer JA, Kosović B, Linn RR (2017) Coupled mesoscale-LES modeling of a diurnal cycle during the CWEX-13 field campaign: from weather to boundary -layer eddies. J Adv Model Earth Syst 9:1572–1594. https://doi.org/10.1002/2017MS000960

Nakanishi M, Niino H (2009) Development of an improved turbulence closure model for the atmospheric boundary layer. J Meteorol Socf Jpn Ser II 87(5):895–912. https://doi.org/10.2151/jmsj.87.895

National Center for Atmospheric Research (2020) Wps v4 geographical static data downloads page. https://www2.mmm.ucar.edu/wrf/users/download/get_sources_wps_geog.html

Olsen BM (2018) Mesoscale to microscale coupling for determining site conditions in complex terrain. PhD thesis, University of Denmark

Quon EW, Ghate AS, Lele SK (2018) Enrichment methods for inflow turbulence generation in the atmospheric boundary layer. J Phys Conf Ser 1037(7):072054. https://doi.org/10.1088/1742-6596/1037/7/072054

Rai RK, Berg LK, Kosović B, Haupt SE, Mirocha JD, Ennis BL, Draxl C (2019) Evaluation of the impact of horizontal grid spacing in Terra Incognita on coupled mesoscale-microscale simulations using the WRF framework. Mon Weather Rev 147(3):1007–1027. https://doi.org/10.1175/MWR-D-18-0282.1

Rhie CM, Chow WL (1983) Numerical study of the turbulent flow past an airfoil with trailing edge separation. AIAA J 21(11):1525–1532. https://doi.org/10.2514/3.8284

Sanz Rodrigo J, Allaerts D, Ávila M, Barcons J, Cavar D, Chávez Arroyo RA, Churchfield MJ, Kosović B, Lundquist JK, Meyers J, Muñoz Esparza D, Palma JMLM, Tomaszewski JM, Troldborg N, van der Laan MP, Veiga Rodrigues C (2017a) Results of the GABLS3 diurnal-cycle benchmark for wind energy applications. J Phys: Conf Ser 854(012):037

Sanz Rodrigo J, Churchfield MJ, Kosović B (2017b) A methodology for the design and testing of atmospheric boundary layer models for wind energy applications. Wind Energy Sci 2:35–54

Schalkwijk J, Jonker HJJ, Siebesma AP, Bosveld FC (2015) A year-long large-eddy simulation of the weather over Cabauw: an overview. Mon Weather Rev 143(3):828–844

Schumann U (1975) Subgrid scale model for finite difference simulations of turbulent flows in plane channels and annuli. J Comput Phys 18(4):376–404. https://doi.org/10.1016/0021-9991(75)90093-5

Skamarock WC, Klemp J, Dudhia J, Gill DO, Barker D, Wang W, Powers JG (2008) A description of the advanced research WRF version 3. National Center for Atmospheric Research, Boulder, CO, Tech Rep NCAR/TN-475+STR

Sprague M, Satkauskas I (2015) Nesting an incompressible-flow code within a compressible-flow code: a two-dimensional study. Comput Fluids 115

Tewari M, Chen F, Wang W, Dudhia J, LeMone MA, Mitchell K, Ek M, Gayno G, Wegiel J, Cuenca RH (2004) Implementation and verification of the unified NOAH land surface model in the WRF model. In: 20th conference on weather analysis and forecasting/16th conference on numerical weather prediction

The OpenFOAM Foundation (2020) OpenFOAM v6 User Guide

Tian L, Song Y, Zhao N, Shen W, Wang T, Zhu C (2020) Numerical investigations into the idealized diurnal cycle of atmospheric boundary layer and its impact on wind turbine's power performance. Renew Energy 145:419–427. https://doi.org/10.1016/j.renene.2019.05.038

Wang W, Bruyére C, Duda M, Dudhia J, Gill D, Kavulich M, Keene K, Chen M, Lin HC, Michalakes J, Rizvi S, Zhang X, Berner J, Ha S, Fossell K, Beezley JD, Coen JL, Mandel J, Chuang HY, McKee N, Slovacek T, Wolff J (2017) User's guide for the advanced research WRF (ARW) modeling system version 3.8

Welch P (1967) The use of fast fourier transform for the estimation of power spectra: a method based on time averaging over short, modified periodograms. IEEE Trans Audio Electroacoust 15(2):70–73

Wu X (2017) Inflow turbulence generation methods. Annu Rev Fluid Mech 49(1):23–49. https://doi.org/10.1146/annurev-fluid-010816-060322

Wyngaard JC (2004) Toward numerical modeling in the "terra incognita". J Atmos Sci 61(14):1816–1826. https://doi.org/10.1175/1520-0469(2004)061<1816:TNMITT>2.0.CO;2

Publisher's Note Springer Nature remains neutral with regard to jurisdictional claims in published maps and institutional affiliations.